Distribution Agreement

In presenting this thesis as a partial fulfillment of the requirements for a degree from Emory University, I hereby grant to Emory University and its agents the non-exclusive license to archive, make accessible, and display my thesis in whole or in part in all forms of media, now or hereafter now, including display on the World Wide Web. I understand that I may select some access restrictions as part of the online submission of this thesis. I retain all ownership rights to the copyright of the thesis. I also retain the right to use in future works (such as articles or books) all or part of this thesis.

Alison Thieberg 4/8/2025

Estimating the Aerosol Direct Radiative Effect Using Different Mixing State Assumptions

by

Alison Thieberg

Alexander Avramov, Ph.D.
Adviser

Environmental Sciences

Alexander Avramov, Ph.D.
Adviser

Eri Saikawa, Ph.D.
Committee Member

Justin Burton, Ph.D.
Committee Member

2025

Estimating the Aerosol Direct Radiative Effect Using Different Mixing State Assumptions

By

Alison Thieberg

Alexander Avramov, Ph.D.
Adviser

An abstract of
a thesis submitted to the Faculty of the Emory College of Arts and Sciences
of Emory University in partial fulfillment
of the requirements for the degree of
Bachelor of Science with Honors

Environmental Sciences

2025

Abstract

Estimating the Aerosol Direct Radiative Effect Using Different Mixing State Assumptions
By Alison Thieberg

Aerosols, whether produced from man-made or natural processes, can impact our climate by altering the radiative balance of the planet. The aerosol direct radiative effect is used to quantify the impact that aerosols have on the incoming and outgoing radiative fluxes of the Earth. Aerosols alter the radiative balance of the Earth by both scattering and absorbing incoming solar radiation, preventing it from warming the planet's surface. The degree to which the aerosols scatter or absorb solar radiation is based on their physical and chemical properties: their mixing state. The mixing state cannot be easily inferred from airborne data, so certain assumptions must be made in regards to the size and chemical mix of the sampled aerosol population. This study compares the direct radiative effect of airborne data using three mixing state assumptions: 1) The aerosols are of the same size and they are fully internally mixed, 2) The aerosols are of different sizes and they are fully internally mixed, and 3) The aerosols are of different sizes and they are fully externally mixed. This study attempts to quantify the difference in the direct radiative effect when these different mixing state assumptions are applied.

Estimating the Aerosol Direct Radiative Effect Using Different Mixing State Assumptions

By

Alison Thieberg

Alexander Avramov, Ph.D.
Adviser

A thesis submitted to the Faculty of the Emory College of Arts and Sciences
of Emory University in partial fulfillment
of the requirements for the degree of
Bachelor of Science with Honors

Environmental Sciences

2025

Acknowledgments

I would like to thank my adviser, Dr. Alexander Avramov, for agreeing to mentor me at the beginning of my junior year and for sticking with me through my entire thesis journey. I gratefully thank Dr. Eri Saikawa and Dr. Justin Burton for agreeing to serve on my committee. I would like to further extend my thanks to Dr. Eri Saikawa for bringing me into her lab and giving me my first exposure to research. I am very grateful to Dr. Andreas Beyersdorf, my adviser during my NASA internship, for initially introducing this research project to me and for letting me expand on it for this thesis. I would additionally like to thank Dr. Shaunna Donaher for sparking my interest in earth sciences and leading me towards this research path. Finally I would like to thank my dear friends Ari Dvorkin, Joshua Gerstenfeld, and Zoe Stephens, as well as my family for their unwavering support during this process.

Contents

List of Figures

List of Tables

List of Acronyms and Symbols

Acronyms

DRE Direct Radiative Effect

BC Black Carbon Aerosols

OA Organic Aerosols

NH_4NO_3 Ammonium Nitrate Aerosols

NO_x Nitrogen Oxides

NH_3 Ammonia

$(NH_4)_2SO_4$ Ammonium Sulfate Aerosols

SO_2 Sulfur Dioxide

FIM Fully Internally Mixed

FEM Fully Externally Mixed

RI Refractive Index

TOA Top Of Atmosphere

SSA Single Scattering Albedo

SARP Student Airborne Research Program

LARGE Langley Aerosol Research Group Experiment

UHSAS Ultra High Sensitivity Aerosol Spectrometer

AMS High-Resolution Time-of-Flight Aerosol Mass Spectrometer

SO_4 Sulfate

NO_3 Nitrate

NH_4 Ammonium

SP2 Single Particle Soot Photometer

TSI TSI-3563 Nephelometer

PSAP Particle Soot Absorption Photometer

AOD Aerosol Optical Depth

AERONET Aerosol Robotic Network

DDA Discrete-Dipole Approximation

RRTM Rapid Radiative Transfer Model

Symbols

ΔF_{aer} Direct Radiative Effect of Aerosols

S_0 Solar Constant

T_{atm} Overlying Atmospheric Transmittance

A_{cld} Cloud Fraction

ΔR Change in Albedo from Aerosol Layer

R_{surf} Surface Albedo

β Upscatter Fraction

τ_{sc} AOD of Scattering Layer

τ_{abs} AOD of Absorbing Layer

τ Total AOD

ω Single Scattering Albedo

λ Wavelength of Solar Radiation

r Aerosol Radius

x Particle Size Parameter

g Asymmetry Parameter

P Phase Function

Q_{sca} Scattering Efficiency

Q_{abs} Absorption Efficiency

Q_{ext} Extinction Efficiency

σ_{sca} Scattering Cross Section

σ_{abs} Absorption Cross Section

σ_{ext} Extinction Cross Section

K_{Σ} Specific Mass Extinction Coefficient

m_L Aerosol Mass Loading

r_{eff} Effective Radius

n Count of Aerosol Particles

m Refractive Index

M_i Mass Fraction

ρ Aerosol Density

mm Molecular Weight

A Absorbance

I Intensity

I_0 Initial Intensity

α Angstrom Exponent

Chapter 1

Introduction

Anthropogenic and natural aerosols impact the planet's radiative balance by interacting with incoming solar radiation and modifying the properties of clouds. Once solar radiation enters the Earth's atmosphere, it encounters aerosols which are solid or liquid particles suspended in the air. Depending on their physical and chemical properties, aerosols can both scatter and absorb this radiation. This is the direct effect of aerosols on the Earth's radiative budget. The aerosols can also modify cloud formation processes which will impact the amount of sunlight scattered by clouds. This is the indirect effect of aerosols. This study will simply focus on the direct effect of aerosols, and specifically, on their instantaneous impact on the Earth's radiative balance. Because the impact of aerosols on the changing climate of the Earth is highly uncertain, it is necessary to work to continue and understand their role in global climate change [5].

The direct radiative effect (DRE) of aerosols is determined by the size and chemical

composition of the aerosols, as well as the thickness of the aerosol layer. The size, amount, and composition of aerosols determine the amount of solar radiation they can scatter back into space (causing a cooling effect) and the amount of radiative energy they can absorb (warming the aerosol layer). Aerosols come in a variety of different chemical species and can find their way into the atmosphere via a multitude of natural or anthropogenic processes. Black carbon aerosols (BC), also known as soot, are a strong absorber of solar radiation and are produced via the incomplete combustion of fuel [6]. Organic aerosols (OA) predominately scatter incoming solar radiation and are produced from the burning of biomass and fossil fuels [7]. Ammonium nitrate aerosols (NH_4NO_3) are strong scatterers and are formed *in-situ* through reactions between nitrogen oxides (NO_x) emitted from vehicles and ammonia (NH_3) coming mostly from dairy and agricultural facilities [8]. Finally, ammonium sulfate aerosols ($(NH_4)_2SO_4$), also strong scatterers, are created by the aqueous or dry oxidation of sulfur dioxide (SO_2) coming from industrial processes and NH_3, again emitted from agricultural sources [9]. Individual aerosol particles can be either composed of a single species, or more commonly they are a mixture of various different types of aerosols. The degree to which a population of aerosols is a combination of multiple species is known as a mixing state. A sample of aerosols can be fully internally mixed (FIM), where each particle is composed of several different aerosol species. The sample could also be fully externally mixed (FEM). In this case each particle is only made of one type of aerosol and the different particles are mixed in the same sample. FIM or FEM populations of aerosols are, in actuality, not very common. The atmosphere is more commonly composed of a combination of these two mixing states, containing some aerosols that are purely one type of aerosol and others that are made of various fractions of aerosols species [10].

The fraction of aerosol species within a given population will alter the properties

of the aerosol layer. The effect that the chemical composition and the size of an aerosol particle has on its optical properties can be understood using Mie theory. Mie theory is an analytical solution to Maxwell's equations, which describes the interactions between electromagnetic radiation and a solid sphere based on the size of the sphere and its unique refractive index (RI) [11]. The magnitude of these interactions is greatest when the size of the sphere is very close to the wavelength of the electromagnetic radiation (resonance effect). Given that typical aerosol sizes are often comparable with the wavelength of incoming solar radiation, this is the case for the aerosol layers in the atmosphere. Although aerosol shapes are not necessarily spherical, it is very common to treat them as spheres for the purposes of Mie calculations. Throughout this thesis, we will adopt this approximation and will assume all aerosol particles to be spherical. The RI of a sample of aerosols is a function of the mixing state of the particles. The chemical composition of an aerosol determines its RI and the RI in conjunction with the particle's size determines its scattering and absorbing efficiencies. These efficiencies can be used to determine the optical properties of the population.

This study intends to apply different mixing state assumptions to airborne aerosol data. We will test three assumptions: 1) The aerosols in the population all have uniform size and the sample is fully internally mixed, 2) The aerosols have different sizes and the sample is fully internally mixed, and 3) The aerosols have different sizes and the sample is fully externally mixed. By using these assumptions we will calculate aerosol optical properties and the direct radiative effect for each method. By comparing the results from the different assumptions, we can understand how the change in the mixing state assumptions alters the aerosol optical properties.

Chapter 2

Methods

2.1 Direct Radiative Effect

Solar radiation enters the Earth's atmosphere and part of it is absorbed by the surface of the planet. The absorbed energy is eventually transferred to the atmosphere. In response to the absorbed solar radiation, the Earth emits the same amount of radiative energy, but in the infrared part of the electromagnetic spectrum in accordance with Wien's law. Thermodynamic laws dictate that the Earth must remain at the same temperature so it achieves equilibrium by emitting as much radiation as it absorbs. Aerosols blocking the solar radiation from reaching the Earth's surface, by either reflecting it back to space or absorbing it, alter the balance of incoming and outgoing fluxes at the top of the atmosphere (TOA). The direct radiative effect (DRE) quantifies this radiative imbalance and helps to estimate the impact of aerosols on the radiative budget of the planet. DRE is defined as the change in the flux divergence at TOA

between the real atmosphere and an aerosol-free atmosphere [5].

When solar radiation reaches the top of the atmosphere, its ability to reach the surface of the Earth is dependent on various parameters, those being: the fraction of clouds in the sky, the ability for light to be transmitted through the atmosphere above the aerosol layer, and the reflectance and absorptivity in the aerosol layer. The following equation by Charlson et al. [12] shows how all of those factors impact the DRE of aerosols (ΔF_{aer}):

$$\Delta F_{aer} = -\frac{S_0}{4} T_{atm}^2 (1 - A_{cld}) \Delta R, \tag{2.1}$$

where $S_0/4$ is the global average of incident solar radiation that reaches TOA. The fraction of incident radiation transmitted by the atmosphere above the aerosol layer is T_{atm} and A_{cld} is the cloud fraction. We use $(1 - A_{cld})$ to isolate cloud-free areas because we are only considering the direct effect of aerosols and not their ability to modify cloud properties. ΔR is the change in the total albedo caused by the aerosol layer. Charlson et al. [12] used the following expression for ΔR which only considered scattering aerosols:

$$\Delta R = (1 - R_{surf})^2 2\beta\tau_{sc}, \tag{2.2}$$

where R_{surf} is the surface albedo, β is the fraction of light scattered by the aerosols back to space, and τ_{sc} is the optical thickness of the scattering layer of aerosols. Chylek and Wong [13] modified ΔR to account for both scattering and absorbing aerosols:

$$\Delta R = (1 - R_{surf})^2 2\beta\tau_{sc} - 4R_{surf}\tau_{abs} \tag{2.3}$$

The addition of the optical thickness of the absorbing layer (τ_{abs}) increases the total aerosol optical thickness. The total optical depth τ is the sum of the scattering

optical depth and the absorption optical depth. Equation 2.3 reduces to equation 2.2 when the aerosol absorptivity is equal to zero. By using the identities $\tau_{sc} = \omega\tau$ and $\tau_{abs} = (1-\omega)\tau$, where ω is the single scattering albedo (SSA), we can rewrite the equation for ΔF_{aer} as:

$$\Delta F_{aer} = -\frac{S_0}{2} T_{atm}^2 (1 - A_{cld})[\beta\omega(1 - R_{surf})^2 - 2(1-\omega)R_{surf}]\tau \tag{2.4}$$

This equation provides us with an analytical way to calculate the DRE for a layer of aerosols. In this study of the DRE, we adopt the following constants as determined by Langride et al. [4]:

$$S_0 = 1366\frac{W}{m^2}, \qquad T_{atm} = 0.76, \qquad A_{cld} = 0, \qquad \text{and} \qquad R_{surf} = 0.14$$

The variables β, ω, and τ cannot be easily measured, but they can be estimated using a combination of observational data and theoretical considerations. In this thesis we are going to implement different methods of estimating the optical properties of an aerosol layer to study their impact on the DRE estimates.

2.2 Mie Theory

The most common way to quantify the relationship between an aerosol and incident solar radiation is by using Gustav Mie's solution to the scattering of light by small particles. While Mie's 1908 theory focused on the scattering by gold particles suspended in water, the mathematical treatment has been adopted by the atmospheric science community for calculating aerosol optics [14]. The theory focuses on spherical particles with a size comparable to that of an incident light's wavelength. Aerosol sizes are on

the same order as the wavelength of visible light, and while they are rarely perfectly spherical, we assume they are to utilize the theory.

To describe the interaction between the sphere and the incoming radiation, Mie theory uses the radius of the aerosol, its refractive index (RI), and the wavelength of the incident radiation. The wavelength (λ) and the radius of the aerosol (r) are combined to create the dimensionless size parameter (x):

$$x = \frac{2\pi r}{\lambda}, \tag{2.5}$$

which is simply the ratio of the aerosol's circumference to λ [15]. The RI of an aerosol particle is a complex number ($m = n - ki$) that describes its interaction with incoming radiation. The real part of the RI represents the aerosol's ability to scatter radiation and the imaginary part represents its ability to absorb radiative energy.

From these inputs we can use Mie theory to calculate various useful aerosol optical properties. The asymmetry parameter (g) is the average cosine of the scattering angle:

$$g = \int_{4\pi} P(\theta) \cos\theta \, d\Omega, \tag{2.6}$$

where P is the phase function. When most of the scattering is in the forward direction, g is greater than 0 and when most of the scattering is in the backward direction, g is less than 0. When g is 0 the scattering is isotropic.

When a photon impinges on an aerosol particle, it will be either scattered or absorbed by the particle. The radiation intensity decrease due to the photons being scattered in a direction different from their initial direction or absorbed is called the extinction or attenuation [11]. We can quantify the degree to which radiative energy is

scattered or absorbed by using Mie theory to calculate the aerosol's efficiencies. The scattering (Q_{sca}), absorption (Q_{abs}), and extinction (Q_{ext}) efficiencies are defined as follows:

$$Q_{sca} = \frac{\sigma_{sca}}{\pi r^2}, \qquad Q_{abs} = \frac{\sigma_{abs}}{\pi r^2}, \qquad Q_{ext} = \frac{\sigma_{ext}}{\pi r^2}, \tag{2.7}$$

where σ_{sca}, σ_{abs}, and σ_{ext} are the scattering, absorption, and extinction cross sections respectively [14]. The efficiencies, as well as the asymmetric parameter, will be used to estimate the upscatter fraction, single scattering albedo, and the optical thickness of the aerosol layer. Given that the computations for finding the efficiencies and the asymmetric parameter are complex and time consuming, we will be using the python package *miepython* developed by Scott Prahl [16].

2.3 Radiative Transfer in Aerosol Layer (β, ω, & τ)

The upscatter fraction (β), single scattering albedo (ω), and aerosol optical depth (τ) are all important optical properties needed to describe to what extent an aerosol layer is scattering and absorbing radative energy. While aerosols scatter radiation in many directions, we denote the amount scattered in the backward hemisphere as β, or the upscatter fraction. β can be found from the parametrization of the Henyey-Greenstein phase function:

$$P(\theta) = \frac{1 - g^2}{(1 + g^2 - 2g\cos\theta)^{3/2}} \tag{2.8}$$

In the calculation of β, Moosmüller and Ogren [15] recommend a third-order polynomial expansion of the integral of the phase function using the asymmetry parameter as the

only argument:

$$\overline{\beta} = -0.2936g^3 + 0.2556g^2 - 0.4489g + 0.5043 \tag{2.9}$$

The single scattering albedo (ω) is the ratio of the scattering efficiency (Q_{sca}) and the total extinction efficiency (Q_{ext}) [17]:

$$\omega = \frac{Q_{sca}}{Q_{ext}}, \tag{2.10}$$

Notice how, given that $Q_{ext} = Q_{sca} + Q_{abs}$, an aerosol that only scatters will have an ω value of 1.

The aerosol optical depth (τ) is the optical thickness of the aerosol layer. It is the sum of both the scattering and absorption layer thicknesses [18]:

$$\tau = \tau_{sca} + \tau_{abs} \tag{2.11}$$

The aerosol optical depth can be numerically calculated using the aerosol specific mass extinction coefficient (K_Σ) and the aerosol mass loading (m_L) [19]:

$$\tau = K_\Sigma \times m_L, \tag{2.12}$$

where m_L is the aerosol mass concentration integrated over the optical path.

The upscatter fraction, SSA, and the aerosol optical depth can all be calculated numerically using the optical properties (g, Q_{sca}, and Q_{ext}) from Mie theory. However, these optical properties are all calculated for a single sphere with a fixed size and chemical composition. In reality, in the same volume of air, aerosols can have different

sizes and chemical compositions. The question that then arises is how can we extend the results for a single sphere to the whole aerosol layer. There are two common methods: 1) Assume a monodisperse aerosol distribution, i.e. all aerosols particles have the same size (effective size) and 2) Integrating the optical properties over the experimentally derived aerosol size distribution.

2.3.1 Monodisperse Size Distribution

The effective-size method considers all aerosols within the population as if they were the same size, i.e. the aerosols are assumed to be mono-dispersed. The first step in doing this is to calculate an effective particle radius (r_{eff}) that can represent the entire sample. Particle size distribution data is obtained through *in-situ* measurements in the aerosol layer. The distribution can be graphed as in Figure 2.1. Thousands of aerosols fly into the inlet of a spectrometer which then sorts them into different bins based on their size. The number of bins is dependent on the precision of the spectrometer. We can use this distribution data to find the effective radius of the distribution. Each bin has a size mid-point with a certain number of aerosol particles (n). Using the height of the bin as a weight we can calculate the weighted radius of the sample:

$$r_{eff} = \sum_i \frac{r_i n_i}{n} \tag{2.13}$$

We use the weighted radius as an effective radius, which can then be used along with the wavelength of the radiation to find the size parameter of the approximated aerosol using Equation 2.5. For the effective-size method we must assume a fully internally mixed population of aerosols since all particles in the population are considered to be the same. Therefore, any data we collect as to the species fraction of the sample,

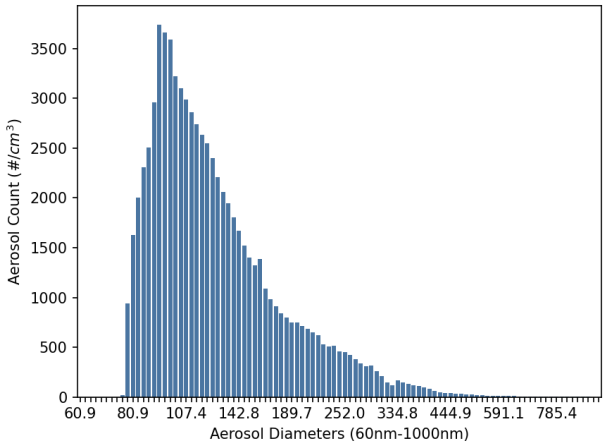

Figure 2.1: Aerosol size distribution data. The distribution is comprised of 99 size bins. The height of each bin is the count of aerosols within the population that correspond to the size of the bin.

we will assume it represents that of all the aerosols. We use this mass fraction to calculate the refractive index of our approximated aerosol sphere. Each aerosol species has a unique refractive index (m) which is experimentally derived using laboratory measurements. Using the mass fractions (M_i) of the sample (visualized in Figure 2.2), we can calculate the weighted refractive index:

$$\mathbb{R}\text{e}(m) = \sum_i \mathbb{R}\text{e}(m_i)M_i, \qquad \mathbb{I}\text{m}(m) = \sum_i \mathbb{I}\text{m}(m_i)M_i \tag{2.14}$$

This will create a unique complex number that represents the effective refractive index of the whole aerosol population reflecting the prevalence of certain species in the aerosol mix.

The weighted refractive index and size parameters are then used to calculate the optical properties of the whole aerosol sample. The asymmetry parameters as well as the scattering and extinction efficiencies are then calculated using Mie theory. This can then be used to find the upscatter fraction and SSA using equations 2.9 and 2.10

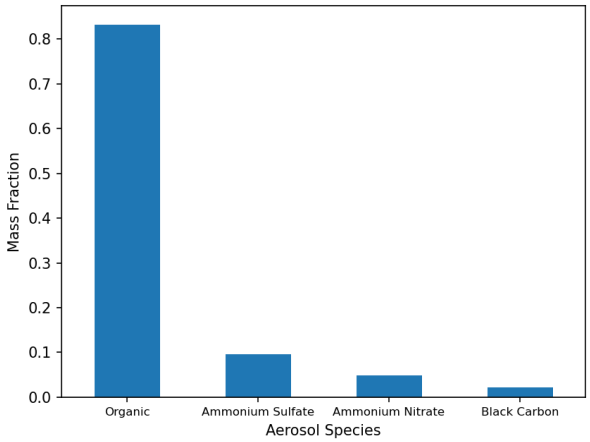

Figure 2.2: The mass fraction of the sample across four aerosol species. The mass fraction is calculated using the airborne mass concentration data.

respectively. To find the specific extinction coefficient per unit mass (K_Σ) for the monodisperse method, we want to use the average density of the aerosol (ρ) along with Q_{ext}:

$$K_\Sigma = \frac{3\pi r_{eff}^2 Q_{ext}}{4\pi\rho r_{eff}^3} = \frac{3Q_{ext}}{4\rho r_{eff}} \tag{2.15}$$

The aerosol optical thickness can then be found by using K_Σ and the aerosol burden of the aerosol column as shown in Equation 2.12.

2.3.2 Integration Over Observed Particle Size Distribution

Instead of representing the entire aerosol population using a single particle with an effective radius, we can find the population optical properties by integrating over the observed aerosol size distribution, thus accounting for their different sizes. The integration techniques will vary depending on the mixing assumptions.

Internally Mixed Similar to the effective-size method, we assume that the mass fraction of all aerosols in the sample is constant. Therefore, we will adopt the weighted refractive index method from Equation 2.14, assuming there is one refractive index that can represent the entire population.

To find ω for the sample, we need to integrate over all aerosol sizes. We do this by finding the Q_{sca} and Q_{ext} values using the weighted RI and the size parameter for each individual bin. These efficiencies, along with the radii and number concentration in each of the bins, are used to find the single scattering albedo:

$$\omega = \frac{\int Q_{sca} r^2 n(r) dr}{\int Q_{ext} r^2 n(r) dr} \tag{2.16}$$

The same methodology is applied when calculating the asymmetry parameter:

$$g = \frac{\int g\, Q_{sca} r^2 n(r) dr}{\int Q_{sca} r^2 n(r) dr}, \tag{2.17}$$

which can then be used to find the upscatter fraction as before.

We calculate K_Σ using the weighted density of the sample. We will estimate the density of the sample using the mass fraction to find a weighted density:

$$\rho = \sum_i \rho_i M_i \tag{2.18}$$

From there we can calculate the specific extinction coefficient per unit mass:

$$K_\Sigma = \frac{3}{4\rho} \frac{\int Q_{ext}\, r^2 n(r) dr}{\int r^3 n(r) dr} \tag{2.19}$$

The optical thickness, τ, can then be easily found using Equation 2.12.

Externally Mixed For a fully externally-mixed aerosol population, we need to calculate all optical properties separately for each aerosol species. Because we need to separate the population by chemical composition, we are using the refractive indices of each species individually. Therefore, the following computations are performed for each species:

$$\omega_j = \frac{\int Q_{sca_j} r^2 n_j(r) dr}{\int Q_{ext_j} r^2 n_j(r) dr}, \tag{2.20}$$

$$g_j = \frac{\int g_j \, Q_{sca_j} r^2 n_j(r) dr}{\int Q_{sca_j} r^2 n_j(r) dr}, \tag{2.21}$$

$$K_{\Sigma_j} = \frac{3}{4\rho_j} \frac{\int Q_{ext_j} \, r^2 n_j(r) dr}{\int r^3 n_j(r) dr}, \tag{2.22}$$

where the index j represents the aerosol species. The extinction coefficients can be used to find the aerosol optical thickness for each species:

$$\tau_j = K_{\Sigma_j} \times m_{L_j} \tag{2.23}$$

The total τ is the sum of the optical thicknesses for each species:

$$\tau = \sum_j \tau_j \tag{2.24}$$

Using τ we can therefore calculate the single scattering albedo and the asymmetry parameter for the entire aerosol layer:

$$\omega = \frac{\sum_j \tau_j \, \omega_j}{\tau} \tag{2.25}$$

$$g = \frac{\sum_j \tau_j \, g_j \, \omega_j}{\tau \, \omega} \tag{2.26}$$

(a) NASA's P-3 Orion Aircraft.

(b) Beechcraft King Air A200.

Figure 2.3: Aircrafts used for airborne data collection during NASA's 2024 SARP flight campaign.

2.4 SARP and Instrumentation

In the summer of 2024 I participated in the NASA Student Airborne Research Program (SARP). Founded in 2009 and based out of the University of California, Irvine, SARP provides undergraduate students the opportunity to participate in airborne data collection and research how the measurements relate to atmospheric, land, and oceanographic processes. We collected data on NASA's P-3 research aircraft, as well as a chartered A200 aircraft. Given that the instrumentation on the A200 focused on collecting whole-air gas samples and not aerosols, we will only be using data from NASA's P-3.

The P-3 was equipped with a suite of instrumentation from NASA's Langley Aerosol Research Group (LARGE). LARGE operated different instrumentation on the P-3, including instruments that measure aerosol particle size, optical properties, and composition. We will be using the data from this suite of instruments to estimate the direct radiative effect of the observed aerosol layer.

Figure 2.4: A UHSAS from Droplet Measurement Technologies [1].

2.4.1 UHSAS

The NASA SARP flights utilized an Ultra High Sensitivity Aerosol Spectrometer (UHSAS) to measure the size of aerosol particles. It measured aerosols ranging in size from 60 nm in diameter to 1000 nm in diameter. NASA's P-3 was outfitted with inlets coming out of repurposed aircraft windows. Aerosols were sampled through the inlet into the main optical system of the UHSAS. Once there, a laser would illuminate the particles, causing them to scatter the light. As we know from Mie theory, the amount of light scattered is related to its size. The intensity of the scattered light acts as a signal to let the UHSAS know the diameter of the particle. Particle sizes are divided into 99 bins, which correspond to diameter ranges. The light signals are relayed to the digital electronics system, which analyzes the peak signals and determines which bin the particle belongs to [1]. The resulting data from the UHSAS is a multitude of bins, each with a specific number concentration (number of particles/cm^3) of aerosols that fall within the bounds of the bin. As we saw in Figure 2.1, this creates a histogram of the aerosol diameter. We used the number concentration and mid-point size of the bin for both the monodisperse method and the integration methods.

2.4.2 AMS

For determining the chemical composition of the aerosols, SARP used a High-Resolution Time-of-Flight Aerosol Mass Spectrometer (AMS). Aerosols from outside the P-3 would enter through an inlet. When they arrive at the AMS they would first go through a beam chopper which would separate the particles by size. The particles enter the mass spectrometer region where they are first vaporized which removes carbon and metals [2]. The remaining particles are then ionized and are accelerated towards the mass spectrometer. The mass spectrometer determines the type of ion and its mass. The AMS onboard the P-3 measures the mass of the sulfate (SO_4), nitrate (NO_3), ammonium (NH_4), and organic aerosol (OA) ions in $\mu g/m^3$. Since the ammonium nitrate (NH_4NO_3) and ammonium sulfate ($(NH_4)_2SO_4$) aerosols were ionized, the AMS will only produce mass concentration data for SO_4, NO_3, and NH_4. We therefore need to calculate the mass concentration of ammonium nitrate and ammonium sulfate using the ion concentrations and the molar mass (mm) of the ions:

$$[(NH_4)_2SO_4] = [SO_4^{2-}] + \frac{[SO_4^{2-}] \div mm_{SO_4} \times 2}{([SO_4^{2-}] \div mm_{SO_4} \times 2) + ([NO_3^-] \div mm_{NO_3})} \times [NH_4^+] \quad (2.27)$$

$$[NH_4NO_3] = [NO_3^-] + \frac{[NO_3^-] \div mm_{NO_3}}{([SO_4^{2-}] \div mm_{SO_4} \times 2) + ([NO_3^-] \div mm_{NO_3})} \times [NH_4^+] \quad (2.28)$$

The mass of the aerosols is used to determine the mass fraction and mass concentration for the population.

Figure 2.5: The AMS by Aerodyne [2].

2.4.3 SP2

Given that the AMS vaporized the elemental carbon aerosols, we used a Single Particle Soot Photometer (SP2) to calculate the mass concentration of black carbon. Black carbon aerosols are strong absorbers of radiation and will transfer this energy to the surounding air after it is absorbed. When black carbon aerosols enter the SP2 they are heated with a laser. They will absorb this energy until they reach the point of incandescence. This process is known as laser-induced incandescence. The black carbon will emit the absorbed energy into the surrounding air mass which will then be measured by the SP2 [3]. Since the peak intensity of the energy is proportional to the black carbon's refractory mass, the SP2 can determine the mass of the particle [20]. The SP2 measures the black carbon mass concentration in ng/m^3. Since the AMS measured aerosol mass concentration in $\mu g/m^3$, the black carbon concentrations were converted to $\mu g/m^3$ so the units would align.

2.4.4 TSI-3563 & PSAP

Though the single scattering albedo is calculated in this study using the size and chemical composition data, we wish to compare those results with the onboard optical

Figure 2.6: The SP2 by Droplet Measurement Technologies [3].

data. The scattering coefficients were measured using a TSI-3563 Nephelometer (TSI). The TSI on the NASA flights measured two types of scattering: total and submicron. The total scattering is the scattering coefficient of the total aerosol sample after being dried. The submicron scattering is the scattering of an aerosol sample that had gone through a 1μm cyclone device. Within the TSI the sample of aerosols is illuminated and the scattering can be viewed against a light trap at the back of the device. The signals of the light scattered by the walls of the TSI as well as the gas inside the instrument are subtracted from the total scattering to isolate the scattering due to aerosols. The TSI records the scattering at three different wavelengths: 450 nm, 550 nm, and 700 nm [21].

The absorption coefficients of the aerosol samples onboard were estimated using a Particle Soot Absorption Photometer (PSAP). When the aerosols enter the PSAP they deposit on a filter. As the aerosols absorb light shone from the instrument, the optical transmission of the filter changes [22]. The absorbance (A) is therefore a function of the intensity of the light initially shone (I_0) and the intensity of the light after being transmitted through the filter (I) as described by Beer's Law:

$$A = \ln \frac{I_0}{I} \tag{2.29}$$

(a) The Integrating Nephelometer 3563 from TSI. Image from LARGE website.

(b) The PSAP from Atmospheric Radiation Measurement (ARM) [22].

Figure 2.7: Optical instruments used on SARP flights.

The PSAP continuously dried the aerosol sample during the measurement process. Similar to the TSI, the PSAP measured at three wavelengths: 470 nm, 532 nm, and 660 nm.

Recall that the single scattering albedo is the ratio of the scattering coefficient to the extinction coefficient, and the extinction coefficient is the sum of the scattering and absorption coefficients. However, the TSI and PSAP measure their respective efficiencies at different wavelengths. To calculate extinction coefficients at 550 nm, the absorption coefficients from the PSAP at 532 nm are adjusted to match the wavelengths of the scattering coefficients using an assumed Angstrom exponent of 1.

2.5 AERONET

We compared the calculated aerosol optical depth (AOD) to the observed AOD at the time of the flights. Though we were able to use onboard data for a comparison of the single scattering albedo as mentioned in the previous section, there are no onboard AOD measurements. We therefore needed to use an external data source to compare our calculated aerosol optical thickness values to. NASA's Aerosol Robotic Network (AERONET) uses ground-based remote sensing technology to monitor the

AOD across the world. AERONET utilizes radiometers that measure the solar flux at ground-level. Using the known top of the atmosphere solar flux, AERONET can infer the thickness of the aerosol layer that is preventing all of the solar flux from reaching the surface of the Earth [23]. AERONET provides data at various different wavelengths, including 440 nm, 500 nm, and 675 nm. Given that we were calculating the AOD at 550 nm, we had to infer the optical thickness (τ) at that wavelength using the Angstrom exponent (α). AERONET provided Angstrom exponent values for 440 nm-675 nm, so we calculated the AOD at 550 nm using those values of α and the AERONET AOD at 440 nm:

$$\tau_{550} = \tau_{440} * \left(\frac{\lambda_{550}}{\lambda_{440}}\right)^{-\alpha_{440-675}} \tag{2.30}$$

The data we used was processed using the AERONET Version 3 algorithm. This version has data at three different quality levels: level 1.0 is raw data, level 1.5 is data that has been screened for clouds, and level 2.0 is data that has been screened for clouds and has been quality assured. Given the scarcity of level 2.0 data for the summer of 2024, we will be using level 1.5 AERONET data in this study.

2.6 Data

The NASA SARP data was first cleaned and divided into flight regions before the optical property estimation techniques were applied. All negative, N/A, or error coded data found in either the size distribution or mass concentration data rendered the observation invalid. Additionally, all values recorded above 1220 m were removed given that we estimate the boundary layer being no higher than 1220 m, and we only wish to focus on the aerosols within the boundary layer. The data was further

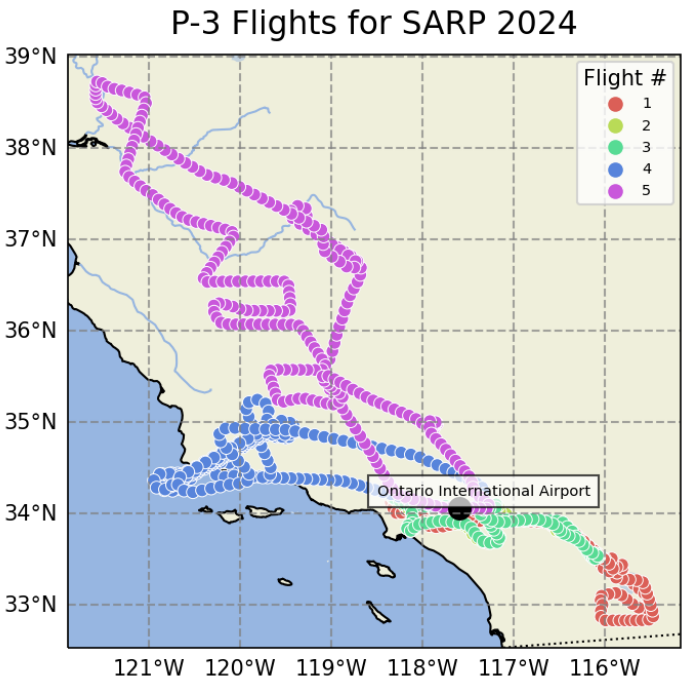

Figure 2.8: The flight paths of the five NASA SARP flights during the 2024 campaign. All flight departed and landed at the Ontario Interntional Airport.

separated by flight and by region.

2.6.1 Flights

The NASA P-3 aircraft engaged in five flights from the Ontario International Airport over the course of three days as seen in Figure 2.8. The goal for this study is to perform the optical property estimation techniques on various columns of air that were sampled. Given that the P-3 flew over various geographic regions during each flight, the data for each flight would be further divided by region. Southern California geography helped to determine the following regions that can be seen in Figure 2.9: The North Central Valley, The South Central Valley, Los Angeles, The Inland Empire, and The Imperial Valley.

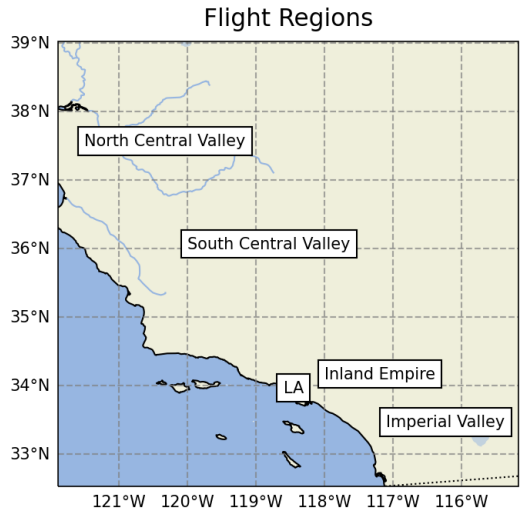

Figure 2.9: The five geographic regions in southern and central California that will determine the location of the air columns. Data from within these regions will be subsetted accordingly.

Column	Flight	Location
1	2	Imperial Valley
2	2	Inland Empire
3	2	Los Angeles
4	3	Imperial Valley
5	3	Inland Empire
6	3	Los Angeles
7	5	North Central Valley
8	5	South Central Valley

Table 2.1: The distinct air columns that include data based on their flight number and their geographic location.

Data from flights that entered the bounds of these regions were divided accordingly. No SP2 data was recorded on flight 1 and the majority of the data recorded on flight 4 was taken at over 1220 m. We therefore will only be dividing the data for flights 2, 3, and 5. The subsetted air columns can be found in Table 2.1.

Chapter 3

Results

This study focuses on aerosols sampled within the boundary layer in Southern California. As discussed previously, the boundary layer height was estimated to be no higher than 1220 m, and thus, all observations above 1220 m were removed. The observations used in the study therefore range from 150 m to 1220 m. The P-3 flew at various altitudes within this range but spent the most time between 400 m and 600 m as can be seen in Figure 3.1. The observations were subsequently divided into air columns based on the flight and the region the aircraft entered. The height of the sampled columns were determined for finding the mass loading. Their altitude ranges are shown in Table 3.1. Given the flight trajectories, the air columns start at various different heights. In some cases like the North Central Valley on the 5th flight and Los Angeles on the 2nd flight, the P-3 was able to sample below 170 m. For all other columns the aircraft could not sample below 280 m.

The altitude ranges are used to find the aerosol mass loading for each column.

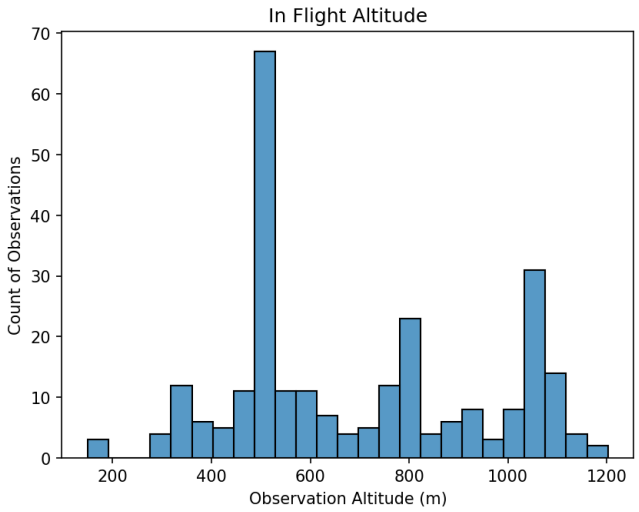

Figure 3.1: The frequency at which observations were recorded at different altitudes for all flights during the NASA SARP 2024 campaign. Observation values we limited to only ones below 1220 m.

Column	Flight	Location	Observation Altitude Range (m)
1	2	Imperial Valley	311 - 1105
2	2	Inland Empire	305 - 1070
3	2	Los Angeles	168 - 1121
4	3	Imperial Valley	283 - 1202
5	3	Inland Empire	398 - 1127
6	3	Los Angeles	358 - 904
7	5	North Central Valley	150 - 1182
8	5	South Central Valley	322 - 871

Table 3.1: Minimum and maximum column height for each column of air across all flights.

The mass loadings for each column can be found in Figure 3.2. Flight 2 in the Inland Empire and in Los Angeles had the highest mass loadings, while flight 2 over the Imperial Valley and flight 3 in the Inland Empire had the lowest mass loadings. The mass loadings are used to calculate the aerosol optical depth (AOD) as given in Equation 2.12.

We can further explore the prevalence of certain aerosol species within the aerosol population. Figure 3.3 shows the fraction of each of the sampled aerosols within the

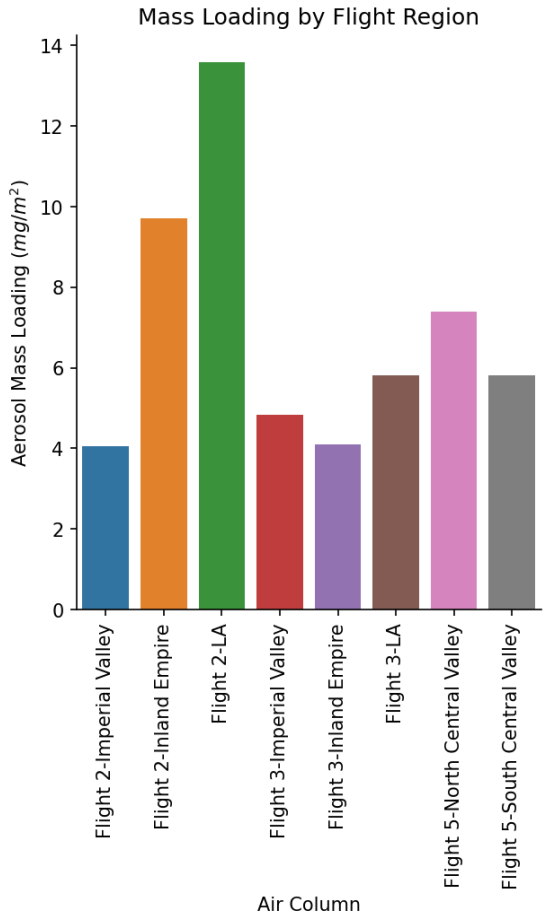

Figure 3.2: The aerosol mass loading (m_L) for all air columns during the SARP 2024 campaign. The m_L was calculated using the height of the air column and the total mass concentration of the column.

column of aerosols. Organics are the most abundant aerosol, followed by ammonium sulfate, ammonium nitrate, and finally black carbon. However, the mass fraction of these aerosol species varies with time and space. As can be seen in Figure 3.3, the prevalence of some of these species fluctuates. For example, organics are more prevalent on flight 5 in the Central Valley but are less so in Los Angeles on flights 2 and 3.

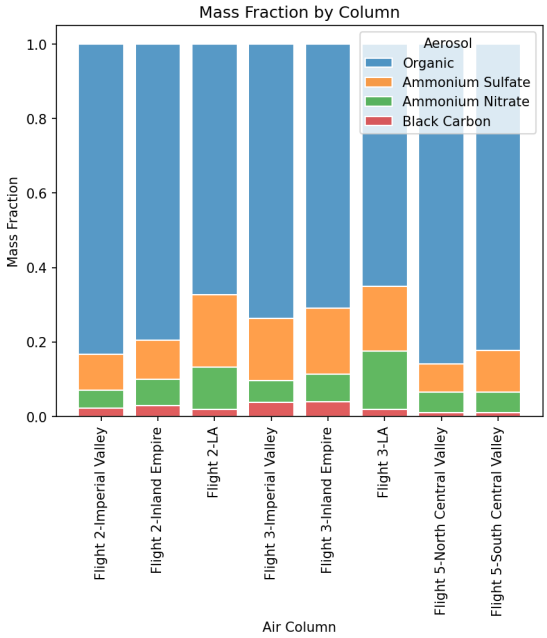

Figure 3.3: The aerosol mass fraction for all air columns. The aerosol mass fraction for each column was calculated using the mass concentration of each of the four aerosol species of interest.

3.1 SSA

The single scattering albedo (SSA) was calculated for each column at 550 nm using the monodisperse method, the integrated internal mix method, and the integrated external mix method. The Langley Aerosol Research Group was able to estimate the dry SSA at 550 nm onboard the P-3 during the flight using data from the TSI and the PSAP. We can therefore compare our calculated SSA values to those of the onboard data. Figure 3.4 shows three plots, each comparing one of the methods for calculating SSA to the onboard SSA. The dashed lines illustrate the desired one-to-one line. By looking at Figure 3.4a one can see that the monodisperse data falls below the line, meaning that Method 1 underestimated the onboard SSA. In Figure 3.4c the integrated external mix data falls above the line, meaning that Method 3 overestimated the SSA values. The results of the integrated internal mix method are closest to the

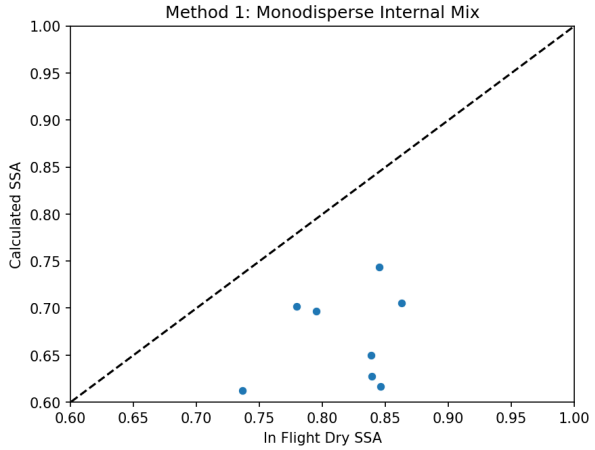

(a) SSA comparison using the monodisperse method.

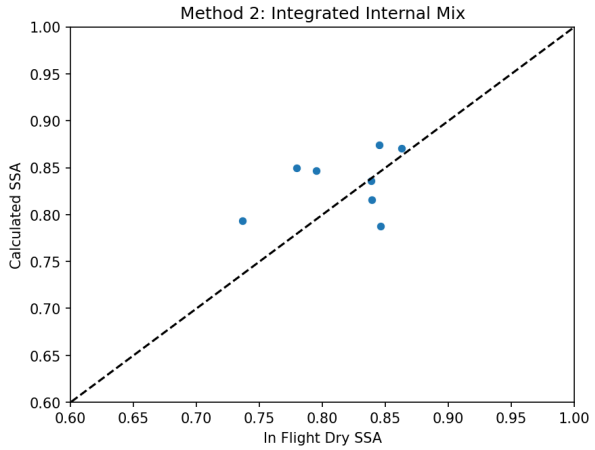

(b) SSA comparison using the integrated internal mix method.

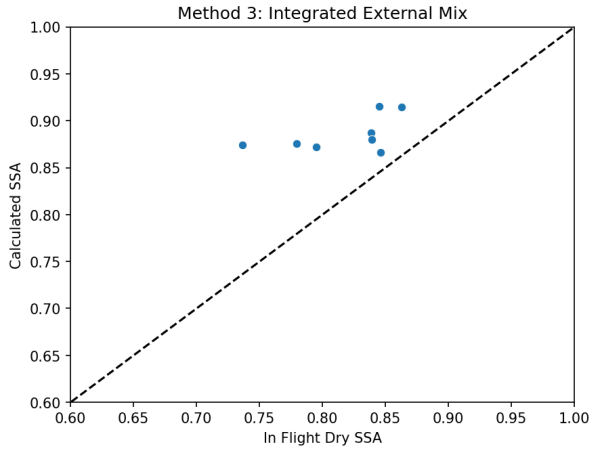

(c) SSA comparison using the integrated external mix method.

Figure 3.4: Single scattering albedo comparisons between the calculated SSA for each method and the onboard dry SSA at 550 nm.

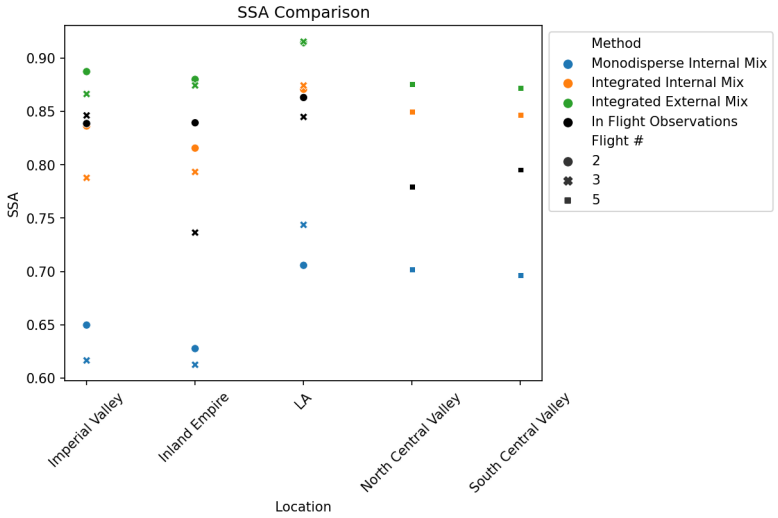

Figure 3.5: Single scattering albedo comparison by geographic location, flight number, and method.

observational data as can be seen in Figure 3.4b.

The performance of the three methods can be further visualized as done in Figure 3.5. The data is separated by regions in the x-axis and by flight from the data point shape. The various colors represent the different mixing state assumptions, with the onboard data in black. This allows us to analyze the distance of the various methods' results from the onboard reference values.

3.2 AOD

Though we cannot compare our calculated AOD data to any onboard flight data, we are able to compare it to ground-based AOD data from AERONET. AERONET stations were selected to correspond to the different geographic regions the aircraft flew through. The locations of the AERONET stations can be found in Figure 3.6 and the flight regions they correspond to can be found in Table 3.2.

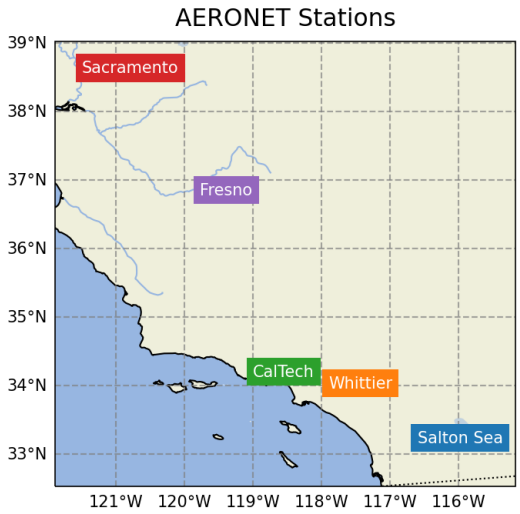

Figure 3.6: The selected AERONET stations in California to be used for comparing the calculated AOD with ground-based AOD.

Region	AERONET Station
Imperial Valley	Salton Sea
Inland Empire	Whittier
LA	CalTech
North Central Valley	Sacramento
South Central Valley	Fresno

Table 3.2: The geographic regions of the study and their assigned AERONET station based on geographic proximity.

Data were queried from the various AERONET stations using the flight's time of entry and exit into the geographic region. Given that the aircraft often spent less than an hour within a flight region, an extra 30 minutes of AERONET data from before the entry and after the exit was used. The time the aircraft spent in the various flight regions can be seen in Table 3.3.

By using AERONET observations we can compare our estimated AOD at 550 nm to the ground-based AOD. Figure 3.7 shows how the AOD values compare with the AERONET data. Each plot shows the optical depth calculations using a different method. The various colors indicate the region/station pairing, and the

Column	Flight	Location	Date	Time Range (PDT)
1	2	Imperial Valley	6/29/24	1:52 PM - 2:06 PM
2	2	Inland Empire	6/29/24	1:31 PM - 2:18 PM
3	2	Los Angeles	6/29/24	1:15 PM - 1:30 PM
4	3	Imperial Valley	7/1/24	8:58 AM - 9:45 AM
5	3	Inland Empire	7/1/24	8:36 AM - 10:01 AM
6	3	Los Angeles	7/1/24	8:16 AM - 8:35 AM
7	5	North Central Valley	7/2/24	10:49 AM - 11:35 AM
8	5	South Central Valley	7/2/24	11:36 AM - 12:54 PM

Table 3.3: The time range and date of the data within each air column.

shapes correlate with the flight number. Again, the dashed one-to-one line helps make a comparison between the ground-based data on the x-axis and the calculated AOD values on the y-axis. AOD values calculated through the monodisperse internal mix method under-predict the AERONET data given that they are far from the one-to-one as can be seen in Figure 3.7a. From Figure 3.7b we see that the integrated internal mix method more closely follows the one-to-one comparison. The integrated external mix method produces very similar AOD values to that of the internal mix method as is shown in Figure 3.7c. Both of these methods over-predict the AOD in Los Angeles on the second flight.

Figure 3.8 illustrates the spread of the estimated AOD from the reference AERONET data in black. The data is divided by flight region and the different flights are once again indicated by shape. Given that the AOD values from the integrated internal mix method and the integrated external mix method are so close, most of the orange symbols are partially or completely covered by the green symbols.

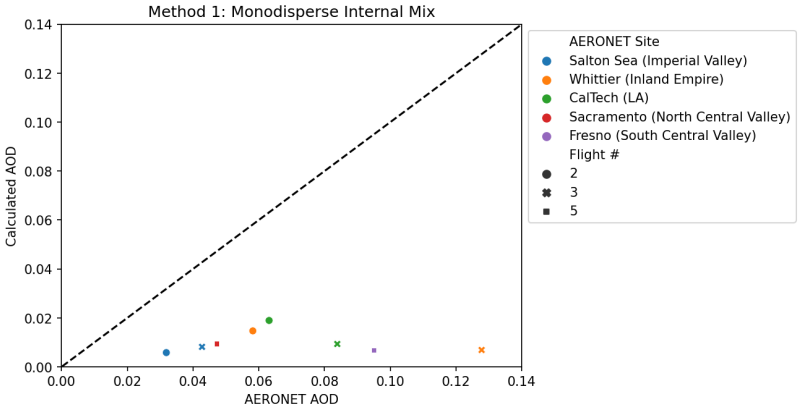

(a) AOD comparison using the monodisperse method.

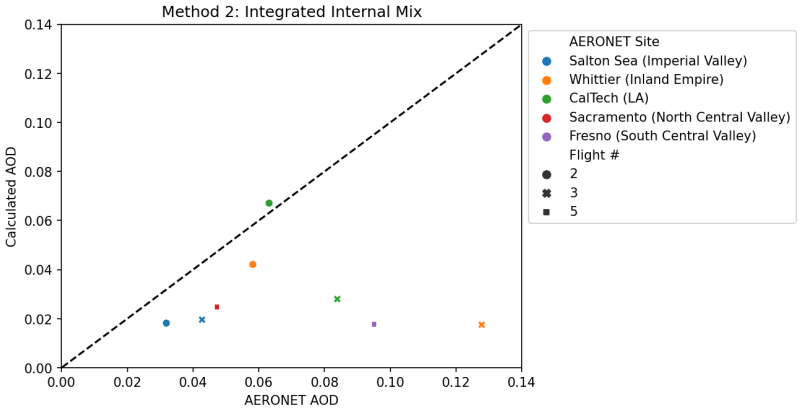

(b) AOD comparison using the integrated internal mix method.

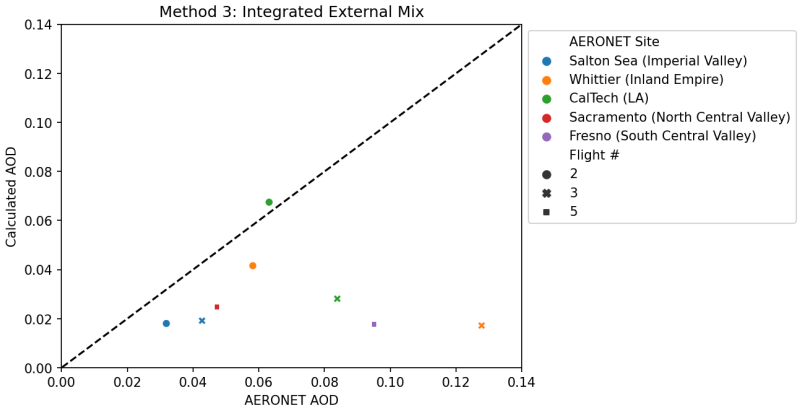

(c) AOD comparison using the integrated external mix method.

Figure 3.7: Aerosol optical depth comparisons between the calculated AOD for each method and the AERONET AOD at 550 nm.

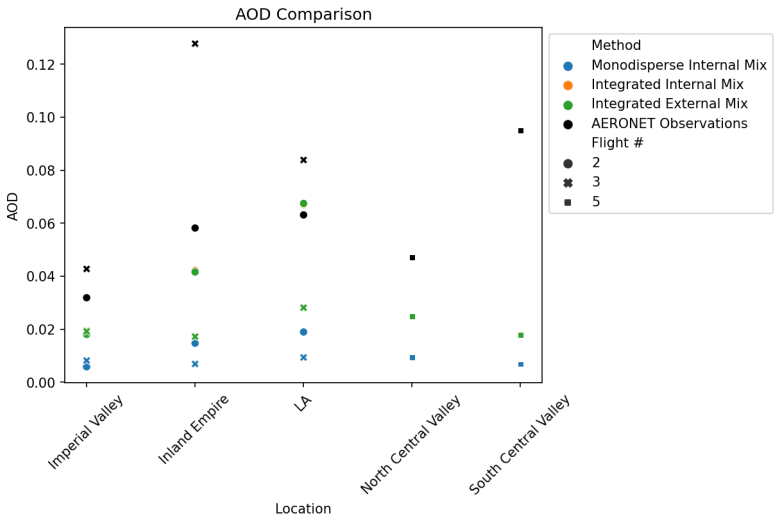

Figure 3.8: Aerosol optical depth comparison by geographic location, flight number, and method.

3.3 DRE

The calculated aerosol optical properties are used to predict the aerosol direct radiative effect using Equation 2.4. For each flight region the ΔF_{aer} was calculated for each method using the method-produced single scattering albedo, upscatter fraction, and AOD. The various DRE values can be seen in Figure 3.9. Each color represents the different methods used and the bars are organized by the air column. Though the bars go above the x-axis, the values on the y-axis are negative.

The AOD that was calculated for each method and applied to the equation for direct radiative effect only represents the section of the aerosol column that the aircraft sampled. The AERONET AOD represents the entire column of air and thus it will be informative to calculate the direct radiative effect using the τ from AERONET. Figure 3.10 shows the direct radiative effect utilizing the τ from AERONET. We can see that by using the τ from AERONET our DRE drastically increases. Only in Los Angeles on flight 2 is the DRE using AERONET smaller than the DRE calculated

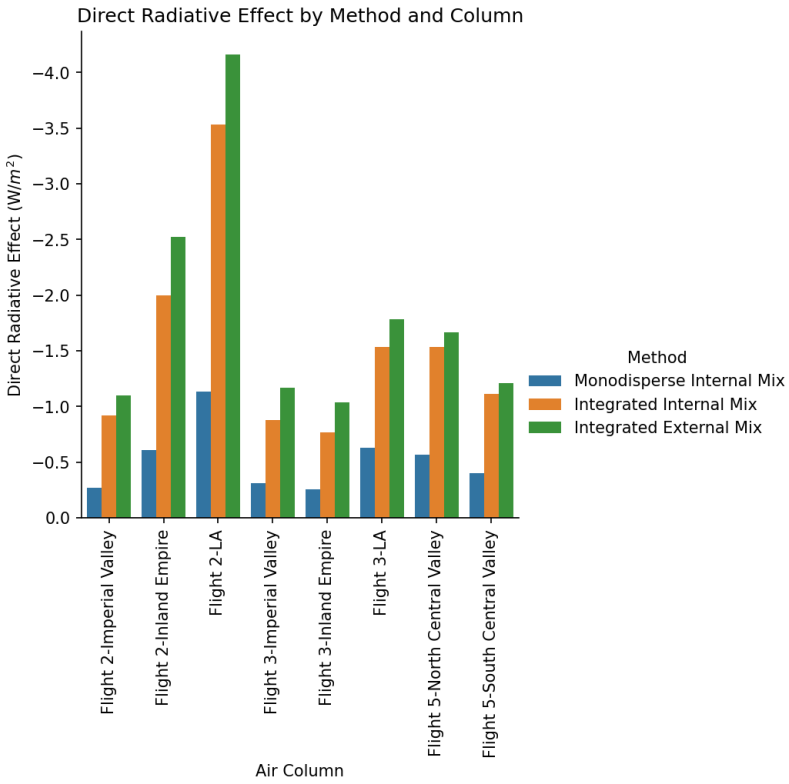

Figure 3.9: The calculated aerosol direct radiative effect across all air columns using the three mixing state assumptions.

without it. This is for both the integrated internal mix method and the integrated external mix method.

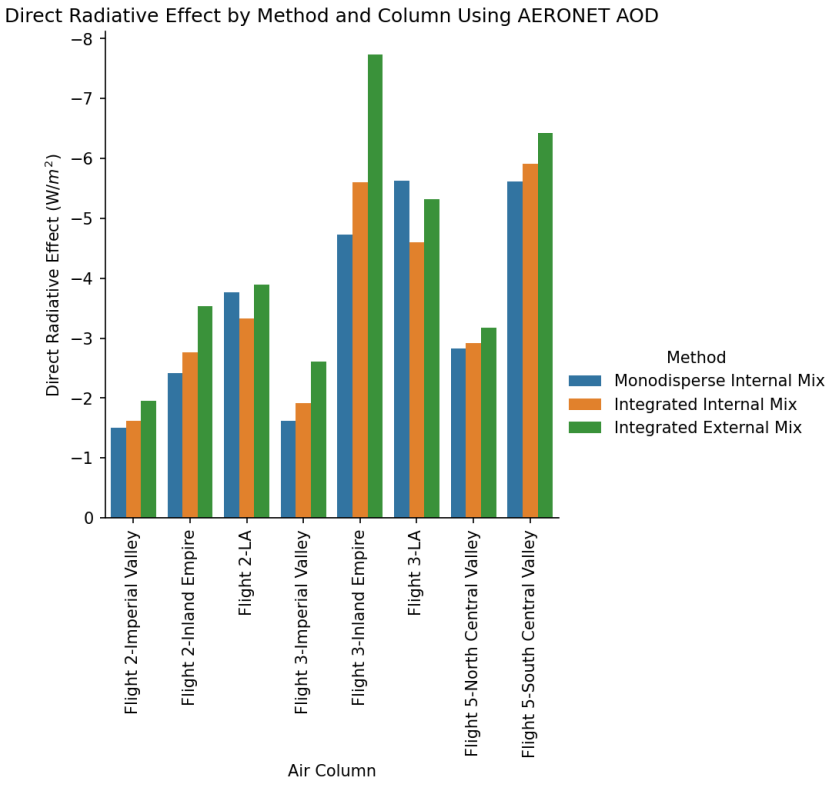

Figure 3.10: The calculated aerosol direct radiative effect across all air columns using the three mixing state assumptions and the τ from AERONET.

Chapter 4

Analysis

4.1 The Impact of the Mixing State

Given the limitations of today's aerosol instrumentation, assumptions must be made in regards to the mixing state of the aerosol population. As we have shown, the three mixing state assumptions tested in this thesis have produced varied SSA, AOD, and DRE values. Figure 3.4 attempts to determine which mixing state assumption matches the sampled aerosol population the best by comparing the calculated SSA to the onboard SSA. The monodisperse method and the integrated internal mix method both assume that the sample is composed of fully internally mixed aerosols. However, the monodisperse method assumes that all aerosols are the same size, while the integrated method acknowledges the size distribution. This has a great impact on the calculated SSA values. Figure 3.4a shows how the monodisperse method underestimates the onboard SSA, while the integrated method more correctly anticipates the magnitude

of the SSA - Figure 3.4b. Assuming that there is one size that represents the aerosol population, versus treating the aerosol size as a distribution, has as great impact on optical properties. The integrated external mix method assumes that the aerosol size is dictated by the size distribution, but that the aerosols are fully externally mixed. This led to the overestimation of the onboard single scattering albedo - Figure 3.4c. The single scattering albedo values might indicate that the integrated internal mix assumption most accurately matches the real mixing state of the sampled aerosol population. The varied values produced using the different mixing state assumptions show how optical properties can differ when certain presumptions are made about an aerosol population.

The varying assumptions have also impacted the calculated aerosol optical depth. Figure 3.7 shows the variation in the estimated AOD values across various methods. The monodisperse method greatly underestimates the ground-based AOD values from AERONET - Figure 3.7a. The integrated internal mix method similarly underestimates the AERONET AOD, however, not to the degree of the monodisperse method - Figure 3.7b. Both methods utilize a weighted refractive index for determining optical properties, but the integrated internal mix method integrated those properties over the size distribution, while the monodisperse method assumes an effective size. This change in the treatment of the size of the aerosol population alters the computed aerosol optical depth. This alteration in assumption proves to be the biggest agent of change for the aerosol optical depth. The AOD calculated using the integrated external mix method produced values that are very similar to those produced by the integrated internal mix method - Figure 3.7c. Both methods integrated optical properties over the size distribution, but the external mix method did so for each aerosol species separately and did not assume a weighted refractive index. This could indicate that, in the case for AOD, it is not the change in assumption of the mix of

the aerosol species that generates the greatest difference, but it is the treatment of the size of the aerosol population. The assumptions made about the mixing state of the aerosol population has a great impact on the resultant AOD calculations.

These varied aerosol optical properties will lead to varied direct radiative effect values. Figure 3.9 illustrates how different mixing state assumptions lead to different aerosol direct radiative effect estimates. The direct radiative effect increases by 194% on average when the mixing state assumptions change from those of the monodisperse method to those of the integrated internal mix method. By simply changing the assumption for the sizes of the aerosols within a population, we are tripling our direct radiative effect. When changing the assumptions regarding how the aerosol species are mixed in the population, the impact is less stark. The integrated external mix method DRE values are on average 19% higher than those of the integrated internal mix method. This coincides with the conclusions previously made regarding the mixing state assumptions impact on the AOD, the size assumption creates the most change. One must proceed with caution when attempting to quantify the direct radiative effect of an aerosol population using real world aerosol data. Making certain conclusions in regards to the size of the population or how the various aerosols species are mixed can greatly vary the results.

4.2 Aerosol Peak Concentrations in the Southern California Basin

As previously mentioned, the aerosol mass loading is the accumulated mass of the aerosol layer through the optical path. As shown in Figure 3.2, the air columns

with the highest mass loading are the ones from flight 2. Flight 2, as Table 3.3 shows, occurred in the afternoon. Aerosol surface emissions peak during times of high transportation, especially in the morning as people are starting their work day. However, those emissions occur at ground-level and take time to mix upward in the atmosphere. By the afternoon, the pollution has mixed in the upper boundary layer. The boundary layer also reaches its maximum height during the late afternoon when the convection is well developed. It would therefore follow that in a city like Los Angeles, famous for its high emissions and overcrowded highways, the highest aerosol mass loading would be observed in the afternoon. From Figure 2.1 we know that the Inland Empire is inland of Los Angeles, and the Imperial Valley is inland of the Inland Empire. The sea breeze circulation can transport pollution from the coast inland. The Los Angeles pollution most likely has been transported through the Inland Empire to the Imperial Valley, decreasing with the distance. This would explain why the Inland Empire and Imperial Valley, regions that don't have nearly as much local emissions as Los Angeles, would have heightened aerosol mass concentrations during this time. The weakening of the transported pollution would also demonstrate how the Inland Empire has a smaller aerosol burden then Los Angeles, and how the Imperial Valley has a smaller aerosol burden then the Inland Empire. A more detailed analysis of the wind trajectories from that flight day using the HYSPLIT model would help to flesh out this conclusion.

In contrast to flight 2, flight 3 followed the same flight path but occurred in the early morning. From Figure 3.2 we notice that the air columns from flight 3 do not follow the same pattern as those from flight 2. Los Angeles still has the highest aerosol burden out of the regions from this flight, but the aerosol burden of the Imperial Valley is lower than that of the Inland Empire. Drawing from our conclusions about the transport of aerosols throughout Southern California, we can infer that there

was no substantial transport bringing pollution from Los Angeles and the aerosol concentrations at the Inland Empire and the Imperial Valley were dominated by local sources. In fact, at night the coast experiences a land breeze circulation which transports air towards the ocean. In addition, this flight took off around 8AM, a time when the mixed boundary layer was still shallow and most likely below the flight altitude. That might explain the lower aerosol concentrations during this flight.

4.3 Single Scattering Albedo

Recall from Equation 2.10 that the single scattering albedo (SSA) is the ratio of the scattering efficiency to the extinction efficiency (scattering + absorption). As the absorption of the aerosol decreases, the SSA approaches 1. The absorption of an aerosol is characterized by the imaginary part of its refractive index. The refractive indices for the sampled aerosol species can be found in Table 4.1. Notice how ammonium nitrate and ammonium sulfate have refractive indices with imaginary parts of 0. This means these aerosols always have an SSA of 1. The single scattering albedo of organic aerosols will be close to 1 given that their refractive index has an imaginary part of 0.02. On the other hand, black carbon, with an imaginary part of 0.79, will have a much lower SSA. For the monodisperse method and the integrated internal mix method, we used the mass fraction to find a weighted refractive index by using Equation 2.14. For the integrated external mix the SSA is weighted by the AOD of each species (Equation 2.20.) Therefore, the mass fraction for each aerosol species is reflected in the single scattering albedo. From looking at Figure 3.5 we can determine which single scattering albedo values are the closest to 1. Across all methods the air columns with the highest SSA were those belonging to Los Angeles on both flights 2 and 3. By looking at Figure

3.3 we can see that the fraction of ammonium nitrate and ammonium sulfate aerosols combined reached a maximum in these air columns. This is why we see such high SSA values for these columns, given that ammonium nitrate and ammonium sulfate only scatter.

We can use the mass fraction to explain other single scattering albedo values as well. The air columns with some of the lowest SSA values across all methods were from flight 3 in the Inland Empire and the Imperial Valley. These columns had the highest mass fractions of black carbon across all observations. Black carbon aerosols are the strongest absorbers of solar radiation as represented by their refractive index of $1.95 - 0.79i$ at 550 nm. A higher fraction of black carbon aerosols within an aerosol population would lead to more absorption of solar radiation and therefore a higher extinction efficiency. Given that the Inland Empire and Imperial Valley on flight 3 have the highest fraction of black carbon as seen in Figure 3.3, we can understand why these columns have such low SSA values. Consider the AOD values for flight 3 calculated in the monodisperse method. As Figure 3.8 shows, all three regions have similar aerosol optical depths, i.e. similar extinctions. However, when comparing the single scattering albedos in Figure 3.5, the single scattering albedo for the flight over Los Angeles is much greater than the SSA values over the Imperial Valley and the Inland Empire. This can be easily explained taking into account that the black carbon mass fraction for the Imperial Valley and the Inland Empire was almost double than that of Los Angeles. Note that the extinction is the sum of the absorption and the scattering. Given that Los Angeles had a higher fraction of scattering aerosols, the extinction was dominated by scattering. On the other hand, the Inland Empire and the Imperial Valley the lower scattering efficiency is compensated by a higher absorption coming from the black carbon.

Aerosol	Refractive Index
Organics	1.63 - 0.02i
Ammonium Nitrate	1.60 - 0.00i
Ammonium Sulfate	1.53 - 0.00i
Black Carbon	1.95 - 0.79i

Table 4.1: Aerosol refractive indices for each species at 550 nm. Values from Langride et al.[4]

4.4 What Impacts the Direct Radiative Effect?

4.4.1 Single Scattering Albedo

A greater single scattering albedo of the aerosol layer will increase the direct radiative effect. As previously mentioned, the integrated internal mix method and the integrated external mix method produce nearly identical values for the aerosol optical thickness. However, Figure 3.9 shows us that the integrated external mix method in this scenario always produces a higher DRE. The higher SSA from the integrated external mix method, as can be seen in Figure 3.5, would explain why that methods' DRE values are the highest. On the other end of the spectrum, the monodisperse method consistently produces the lowest direct radiative effect. While the monodisperse method has the lowest AOD values, as shown in Figure 3.8, it also has by far the lowest single scattering albedo values. This is just one of the variables that has a great impact on the direct radiative effect.

4.4.2 Optical Thickness

The optical thickness also has a great impact on the direct radiative effect. Figure 3.9 and 3.10 both use the method produced upscatter fraction and single scattering albedo. However, 3.9 uses the method produced AOD and 3.10 uses the AERONET AOD. For almost all air columns, the AERONET τ is greater than the one calculated because the aircraft only sampled a limited fraction of the vertical column and the AERONET retrieved AOD is representative for the entire column. Due to flight restrictions that prevented the aircraft from flying at low altitudes, we are underestimating the true aerosol optical depth. The higher AOD from AERONET dramatically increases the direct radiative effect. Accurate estimates of the aerosol direct radiative effect are reliant on an AOD that is representative of the entire column of air.

4.4.3 Surface Albedo

Let us analyze how a changing surface albedo could impact the aerosol direct radiative effect. Up until now we have only been considering R_{surf} as a constant. However, surface albedo varies greatly between different geographic regions. Thus, we want to see what the direct radiative effect would be if we place our air columns in a different location. Recall that our estimate of the surface albedo for California is 0.14. What happens if we increase the surface albedo? Consider the famous salt flats of Bolivia, the *Salar de Uyuni*. Their bright white color gives them a particularly reflective quality. This region has an incredibly high albedo, estimated to be 0.69 [24]. Figure 4.1 illustrates the direct radiative effect of our air columns when placed in the Bolivian salt flats. Notice how the direct radiative effect for all columns is now positive. This is because the aerosol layer is blocking solar radiation for being reflected back to space

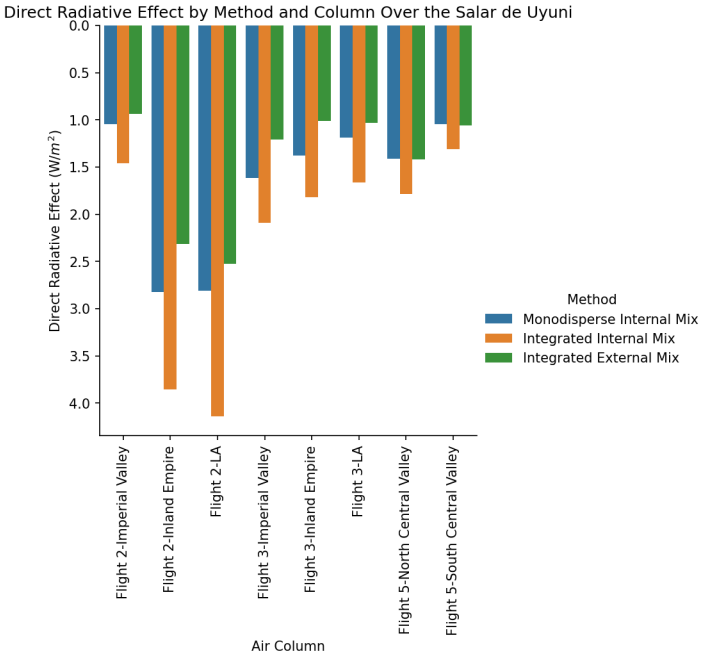

Figure 4.1: The calculated aerosol direct radiative effect across all air columns using the three mixing state assumptions and the surface albedo of the *Salar de Uyuni*.

by the highly reflective salt flats. Recall that the aerosol direct radiative effect is defined as the net short-wave flux difference at the top of the atmosphere between an atmosphere devoid of aerosols and an atmosphere with aerosols. If a planet with an aerosol layer can reflect more radiation back to space than it could if there was no aerosol layer, the direct radiative effect is negative. If an aerosol-free planet can reflect more radiation back to space than if there was a layer of scattering aerosols, the direct radiative effect is positive. In the case of the salt flats, we observe a positive direct radiative effect. For our air columns we will see a greater upward flux if there were no aerosols in the atmosphere. In this case we see the direct radiative effect is greater for the integrated internal mix method than it is for the integrated external mix method. This is because the single scattering albedo from the internal mix assumption is less than the single scattering albedo from the external mix assumption. The higher single scattering albedo means more cooling from the aerosol layer, decreasing the warming effect of an aerosol layer over an area with a high surface albedo.

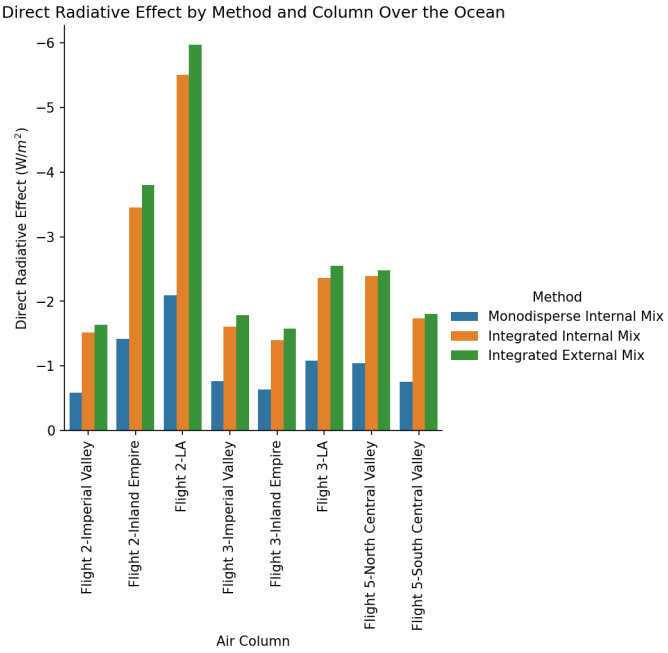

Figure 4.2: The calculated aerosol direct radiative effect across all air columns using the three mixing state assumptions and the surface albedo of the ocean.

Now let's consider a scenario with a surface albedo lower than 0.14. The albedo of the ocean ranges with the solar zenith angle, white cap formation, and wind trajectories. However, given its dark color, on days with clear skies the ocean is estimated to have a surface albedo of 0.03 [25]. Figure 4.2 demonstrates the direct radiative effect of our columns if they were moved over the open ocean on a clear day. Notice how the fluxes are higher than those from Figure 3.9 where the surface albedo was higher. This is because a planet with a lower surface albedo does not scatter as much radiation back to space as if there were an aerosol layer. We can see how the direct radiative effect therefore increases as we decrease the albedo of the surface.

4.5 Limitations

4.5.1 Instrumentation

The Aerosol Mass Spectrometer (AMS) used onboard the P-3 only determined the mass concentration of a limited set of aerosol species for the 2024 SARP flight campaign. While the four species detected by the AMS are ever present in our modern world and contribute greatly to the aerosol optical thickness, they are not the only aerosol species which make up the aerosol layer. Notably missing from the aerosol mass concentration data are the mineral dust aerosols and sea salt aerosols. Dust and sea salt, both natural aerosols, can enter the atmosphere via a multitude of processes. For example, heightened surface winds over a desert or the breaking of ocean waves. These species contribute greatly to the global aerosol optical thickness [26]. Given that this study was conducted using data from California, a region known for big waves and dusty valleys, we are underestimating the thickness of our aerosol layer by disregarding them. For future studies in this region, attempts should be made to determine the mass of these two aerosol species.

Given that we are not considering the presence of dust or sea salt, we are underestimating the mass concentration of the aerosol layer. Recall that the mass concentration data and the size distribution data came from different pieces of instrumentation. Our calculations assumed that the mass concentrations from the AMS represent the aerosols from the size distribution data. However, we can never be certain that this was indeed the case. Furthermore, given the prevalence of other aerosols in the Southern California basin, the aerosol mass distribution likely contains dust and sea salt aerosols. This would mean that only a fraction of our initial size distribution

contains the aerosol species sampled on the AMS. Applying the mass fraction data for four aerosol species to a size distribution that contains a multitude of different species would mean that we disregard the impact of other species on the make-up of the distribution. A more robust AMS setup that considered a wide variety of aerosol species would help narrow the gap between the scope of the mass data and the scope of the distribution data.

In this study we attempted to measure the performance of the various methods by comparing the calculated SSA values to the SSA data from the P-3. However, we must not be quick to assume that the onboard single scattering albedo data is the standard. Recall that the single scattering albedo was not directly measured on the P-3. The values were later calculated using the data from other pieces of optical instrumentation. The SSA at $550nm$ was calculated using scattering data from the TSI and absorption data from the PSAP. However, while the TSI recorded scattering at $550nm$, the closest wavelength the PSAP recorded absorption at was $532nm$. The absorption data had to be corrected using an assumed Angstrom exponent value of 1. Given that the single scattering albedo was not directly recorded, but rather calculated using different pieces of equipment and mathematical corrections, we should caution ourselves before assuming that the SSA data is a standard that our calculations should be compared to.

4.5.2 Assumptions

The computations performed in this study were done under the assumption that the aerosols within the population were perfectly spherical. Mie theory is only used for perfect spheres, which is why we assumed that our aerosols were spherical so we could

make use of the theory. However, aerosols (especially black carbon), are rarely perfect spheres. There exist other light scattering theories that would be more appropriate for aerosols of arbitrary shape. One such method is the discrete-dipole approximation (DDA) which uses polarizable dipoles to approximate the continuum target [27]. The DDA is suitable for spherical and non-spherical particles, becoming particularly useful for the field of aerosol physics. Given that the non-spherical black carbon aerosol is of keen interest within this study, the use of DDA for estimating optical properties could provide more realistic results.

When computing the aerosol mass loading for the various columns of air, we assumed that the air column consisted of one well-mixed layer that spanned from the lowest observation to the highest observation. However, aerosol layers are often not as large as the height of the sampled column of air. Within the column there could be pockets of high aerosol concentration and regions where there are none. A more appropriate technique would be to divide the column of air into layers of equal thickness. The aerosol loading would be calculated for each layer individually, and would then be summed up to find the aerosol burden of the column. This would essentially weight the aerosol loading by the mass concentration within the layers. This approach would provide a more realistic AOD estimate since it better accounts for aerosol vertical distribution.

Within this study we only considered two assumptions in regards to the mix of the aerosol species. Our monodisperse and integrated internal mix methods assume that the aerosol species are fully mixed within the individual aerosols, while our integrated external mix method assumes that each aerosol is composed of only one species. However, as previously mentioned, these two scenarios are hardly found in nature. A more appropriate mixing state assumption would be one consisting of both

internally and externally mixed aerosols. Future works will include experimenting with various real-world mixing state assumptions and comparing those results to those of the previous methods, as well as the onboard SSA and the ground-based AERONET data.

When calculating optical properties within this study we assumed that the only radiation interacting with the aerosols was that which had a wavelength of $550nm$. This assumption was made given that the solar radiation spectrum has a peak at about $550nm$. However, the sun emits radiation at more than just one wavelength, and these various wavelengths of radiation will have different interactions with our aerosols per Mie theory. For us to truly understand the aerosol direct radiative effect of our population, we must consider the interactions of the aerosols with all wavelengths of solar radiation. The more appropriate approach would be to involve a radiative transfer model such as Rapid Radiative Transfer Model (RRTM) which would integrate the incoming and outgoing radiative fluxes over the entire spectral distribution throughout the whole depth of the atmosphere [28]. Next steps for this study would be to use a RRTM to account for all wavelengths of solar radiation and their interactions with aerosols.

Chapter 5

Conclusion

Airborne aerosol data can be used to determine the aerosol direct radiative effect of the aerosol population. The optical properties used to compute the direct radiative effect are a product of the aerosol population's mixing state, the degree to which various aerosols species are mixed within a population. The airborne aerosol data collected from SARP NASA flights does not indicate the aerosol mixing states of the observations. Therefore, we must make assumptions about the sizes of the aerosols and how different species in the population are mixed in order to understand the direct radiative effect of the population. We tested three assumptions: 1) The aerosols all had the same size and the species were fully mixed within the particles, 2) The aerosols had different sizes and the species were fully mixed within the particles, and 3) The aerosols had different sizes and each aerosol was composed of only one species. The assumptions were applied to data from 8 aerosol layers that were created from the airborne data based on the flight number and location of the observation. For the first assumption we used the size distribution data to calculate an effective

aerosol size and we assumed all particles have this size. We assumed all aerosol species are fully internally mixed within each particle and used the mass fraction data to calculate a weighted refractive index to represent the population. The effective size and weighted refractive index were used with Mie theory to find the optical properties of the population. For the second assumption we once again used the weighted refractive index given that we were assuming our population to be internally mixed. However, because the second assumption assumes that the aerosols have different sizes as indicated by the size distribution, we found the optical properties for each size bin using the weighted refractive index and then integrated over the entire distribution. For the third assumption we assumed the particles to be fully externally mixed, so we no longer used the weighted refractive index. Instead we calculated the optical properties of each of the species separately using their refractive indices and those individual optical properties were used to find the optical properties of the entire population. The optical properties were then used to calculate the aerosol direct radiative effect. The three methods produced varied aerosol direct radiative effect values. The average DRE for the second method was 194% higher than that of the first and the average DRE for the third method was 19% higher than that of the second. The results from this study help to understand the impact that the presumptions made about an aerosol population's mixing state can have on its optical properties. The assumptions made in regards to the mixing state are not arbitrary: they can drastically change the estimated aerosol direct radiative effect. Therefore, a proper estimation of the direct radiative effect requires the use of mixing state assumptions that best suit the aerosol population. It would be ideal if the mixing state for every sampled aerosol population could be easily identified. However, the field of aerosol sampling is simply not there yet. Until then, we must be mindful when attempting to calculate the direct radiative effect using airborne data. Careful consideration must be made as to what mixing state assumptions best fit the population in question. In

order to understand the impact that aerosols exert on the Earth's climate, in addition to the question 'how many aerosols are out there,' we also have to ask, 'how is the aerosol layer mixed?'

5.1 Acknowledgments

The airborne aerosol data used in this study was recorded and compiled by the NASA Langley Aerosol Research Group. Access to this data was made possible by my participation in the NASA SARP 2024 cohort.

The ground-based AOD data was recorded and distributed online by the PIs at the following AERONET stations: CalTech, Salton Sea, WC Whittier CA, Fresno 2, and Sacramento CARB.

Chapter 6

Appendix

6.1 Code Processing Diagrams

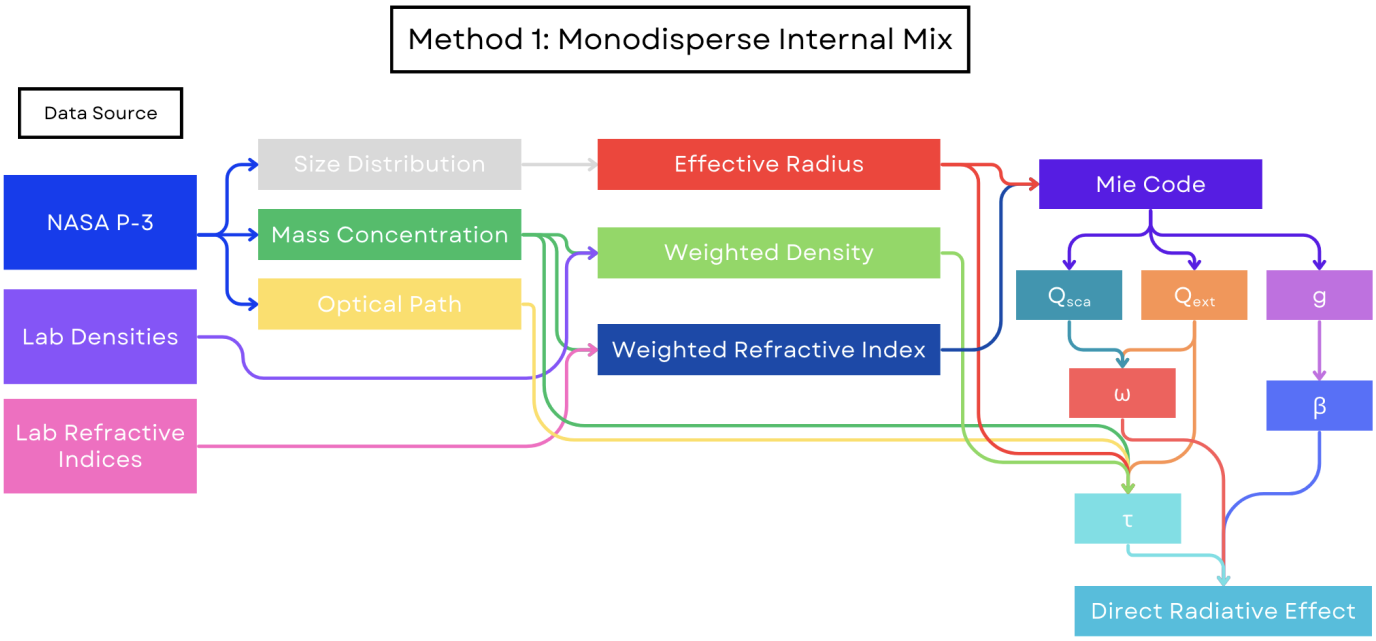
Method 1: Monodisperse Internal Mix
Data Source
NASA P-3
Lab Densities
Lab Refractive Indices
Size Distribution
Mass Concentration
Optical Path
Effective Radius
Weighted Density
Weighted Refractive Index
Mie Code
Qsca
Qext
g
ω
β
τ
Direct Radiative Effect

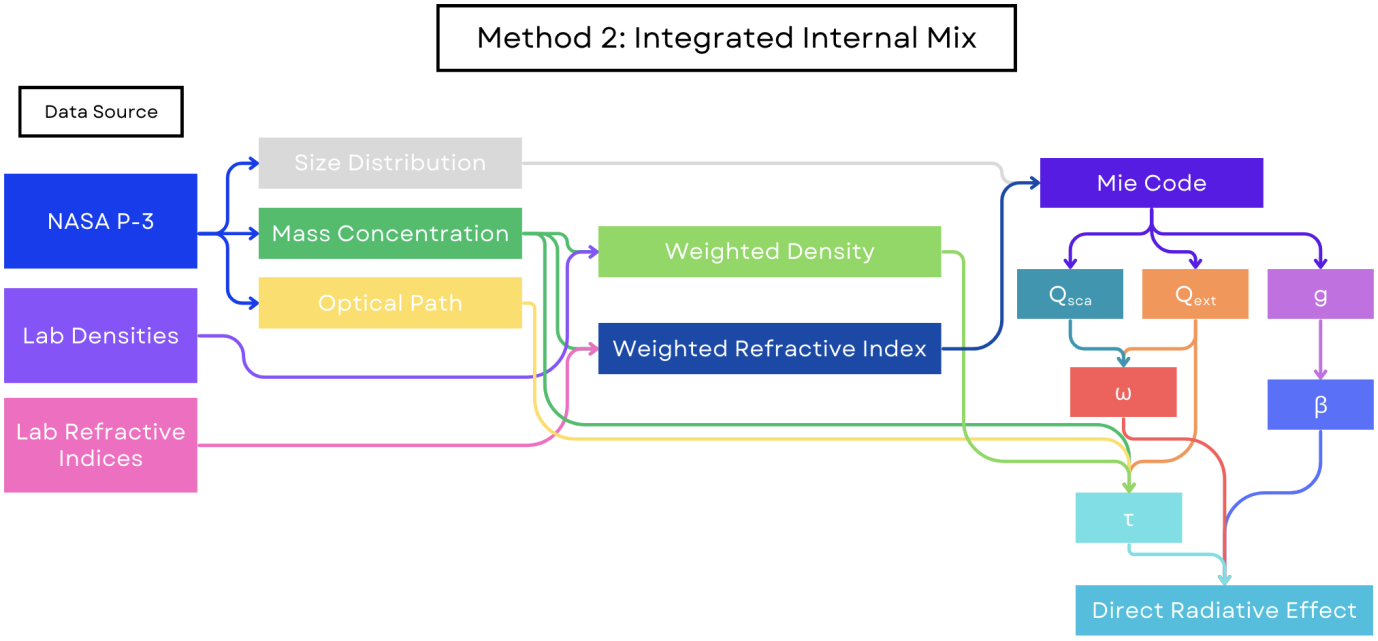
Method 2: Integrated Internal Mix
Data Source
NASA P-3
Lab Densities
Lab Refractive Indices
Size Distribution
Mass Concentration
Optical Path
Weighted Density
Weighted Refractive Index
Mie Code
Qsca
Qext
g
ω
β
τ
Direct Radiative Effect

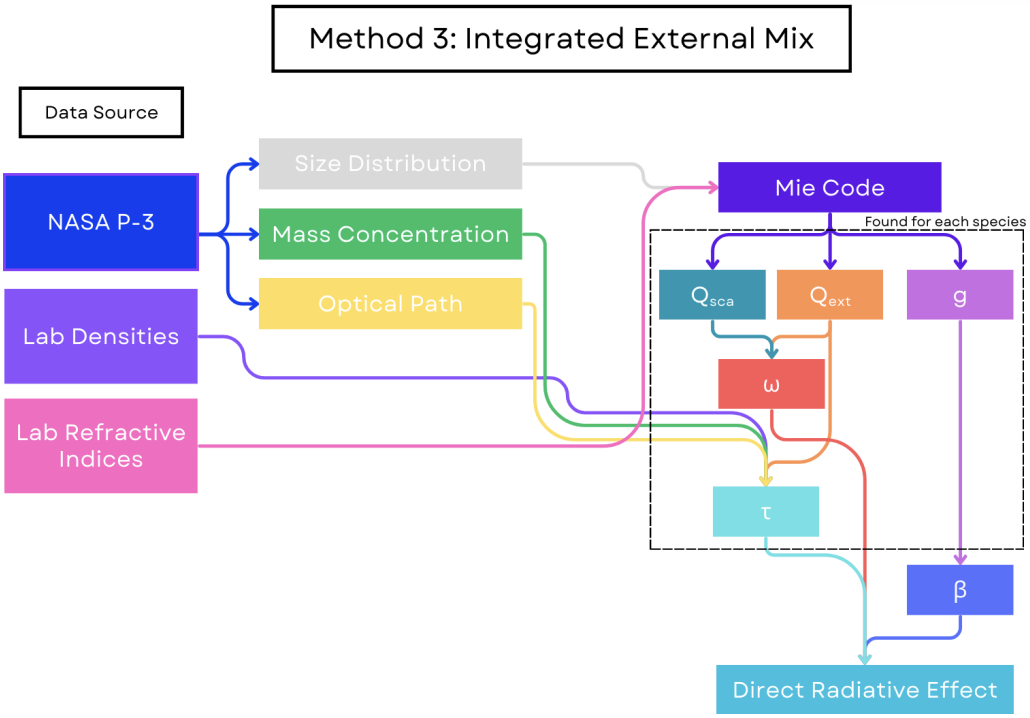
Method 3: Integrated External Mix
Data Source
NASA P-3
Lab Densities
Lab Refractive Indices
Size Distribution
Mass Concentration
Optical Path
Mie Code
Found for each species
Qsca
Qext
g
ω
τ
β
Direct Radiative Effect

Bibliography

[1] Droplet Measurement Technologies. Ultra High Sensitivity Aerosol Spectrometer (UHSAS), 2017.

[2] Aerodyne. Aerosol Mass Spectrometer Systems.

[3] Droplet Measurement Technologies. Single Particle Soot Photometer (SP2), 2022.

[4] Justin M. Langridge, Daniel Lack, Charles A. Brock, Roya Bahreini, Ann M. Middlebrook, J. Andrew Neuman, John B. Nowak, Anne E. Perring, Joshua P. Schwarz, J. Ryan Spackman, John S. Holloway, Ilana B. Pollack, Thomas B. Ryerson, James M. Roberts, Carsten Warneke, Joost A. De Gouw, Michael K. Trainer, and Daniel M. Murphy. Evolution of aerosol properties impacting visibility and direct climate forcing in an ammonia-rich urban environment. *Journal of Geophysical Research: Atmospheres*, 117(D21):2011JD017116, November 2012.

[5] C. L. Heald, D. A. Ridley, J. H. Kroll, S. R. H. Barrett, K. E. Cady-Pereira, M. J. Alvarado, and C. D. Holmes. Contrasting the direct radiative effect and direct radiative forcing of aerosols. *Atmospheric Chemistry and Physics*, 14(11):5513–5527, June 2014.

[6] T. Novakov, V. Ramanathan, J. E. Hansen, T. W. Kirchstetter, M. Sato, J. E. Sinton, and J. A. Sathaye. Large historical changes of fossil-fuel black carbon aerosols. *Geophysical Research Letters*, 30(6):2002GL016345, March 2003.

[7] Qi Zhang, Jose L. Jimenez, Manjula R. Canagaratna, Ingrid M. Ulbrich, Nga L. Ng, Douglas R. Worsnop, and Yele Sun. Understanding atmospheric organic aerosols via factor analysis of aerosol mass spectrometry: a review. *Analytical and Bioanalytical Chemistry*, 401(10):3045–3067, December 2011.

[8] J. B. Nowak, J. A. Neuman, R. Bahreini, A. M. Middlebrook, J. S. Holloway, S. A. McKeen, D. D. Parrish, T. B. Ryerson, and M. Trainer. Ammonia sources in the California South Coast Air Basin and their impact on ammonium nitrate formation. *Geophysical Research Letters*, 39(7):2012GL051197, April 2012.

[9] J. M. Walker, S. Philip, R. V. Martin, and J. H. Seinfeld. Simulation of nitrate, sulfate, and ammonium aerosols over the United States. *Atmospheric Chemistry and Physics*, 12(22):11213–11227, November 2012.

[10] N. Riemer, A. P. Ault, M. West, R. L. Craig, and J. H. Curtis. Aerosol Mixing State: Measurements, Modeling, and Impacts. *Reviews of Geophysics*, 57(2):187–249, June 2019.

[11] Helmuth Horvath. Gustav Mie and the scattering and absorption of light by particles: Historic developments and basics. *Journal of Quantitative Spectroscopy and Radiative Transfer*, 110(11):787–799, July 2009.

[12] R. J. Charlson, S. E. Schwartz, J. M. Hales, R. D. Cess, J. A. Coakley, J. E. Hansen, and D. J. Hofmann. Climate Forcing by Anthropogenic Aerosols. *Science*, 255(5043):423–430, January 1992. Publisher: American Association for the Advancement of Science.

[13] Petr Chylek and J. Wong. Effect of absorbing aerosols on global radiation budget. *Geophysical Research Letters*, 22(8):929–931, April 1995.

[14] Craig F. Bohren and Donald R. Huffman. *Absorption and Scattering of Light by Small Particles*. April 1998.

[15] Hans Moosmüller and John A. Ogren. Parameterization of the Aerosol Upscatter Fraction as Function of the Backscatter Fraction and Their Relationships to the Asymmetry Parameter for Radiative Transfer Calculations. *Atmosphere*, 8(8):133, July 2017.

[16] Scott Prahl. miepython: Pure python calculation of Mie scattering, August 2023.

[17] T. L. Anderson, D. S. Covert, J. D. Wheeler, J. M. Harris, K. D. Perry, B. E. Trost, D. J. Jaffe, and J. A. Ogren. Aerosol backscatter fraction and single scattering albedo: Measured values and uncertainties at a coastal station in the Pacific Northwest. *Journal of Geophysical Research: Atmospheres*, 104(D21):26793–26807, November 1999.

[18] R. J. Charlson, J. Langner, H. Rodhe, C. B. Leovy, and S. G. Warren. Perturbation of the northern hemisphere radiative balance by backscattering from anthropogenic sulfate aerosols*. *Tellus A*, 43(4):152–163, August 1991.

[19] Jianbing Jin, Bas Henzing, and Arjo Segers. How aerosol size matters in aerosol optical depth (AOD) assimilation and the optimization using the Ångström exponent. *Atmospheric Chemistry and Physics*, 23(2):1641–1660, January 2023.

[20] J. P. Schwarz, R. S. Gao, D. W. Fahey, D. S. Thomson, L. A. Watts, J. C. Wilson, J. M. Reeves, M. Darbeheshti, D. G. Baumgardner, G. L. Kok, S. H. Chung, M. Schulz, J. Hendricks, A. Lauer, B. Kärcher, J. G. Slowik, K. H. Rosenlof, T. L. Thompson, A. O. Langford, M. Loewenstein, and K. C. Aikin. Single-particle measurements of midlatitude black carbon and light-scattering aerosols from the boundary layer to the lower stratosphere. *Journal of Geophysical Research: Atmospheres*, 111(D16):2006JD007076, August 2006.

[21] TSI. 3563 Integrating Nephelometer, 2002.

[22] Stephen Springston. Particle Soot Absorption Photometer (PSAP) Instrument Handbook, May 2018.

[23] B.N. Holben, T.F. Eck, I. Slutsker, D. Tanré, J.P. Buis, A. Setzer, E. Vermote, J.A. Reagan, Y.J. Kaufman, T. Nakajima, F. Lavenu, I. Jankowiak, and A. Smirnov. AERONET—A Federated Instrument Network and Data Archive for Aerosol Characterization. *Remote Sensing of Environment*, 66(1):1–16, October 1998.

[24] Joachim Reuder, Flavio Ghezzi, Eduardo Palenque, Rene Torrez, Marco Andrade, and Francesco Zaratti. Investigations on the effect of high surface albedo on erythemally effective UV irradiance: Results of a campaign at the Salar de Uyuni, Bolivia. *Journal of Photochemistry and Photobiology B: Biology*, 87(1):1–8, April 2007.

[25] Zhonghai Jin, Thomas P. Charlock, William L. Smith, and Ken Rutledge. A parameterization of ocean surface albedo. *Geophysical Research Letters*, 31(22):2004GL021180, November 2004.

[26] Ina Tegen, Peter Hollrig, Mian Chin, Inez Fung, Daniel Jacob, and Joyce Penner. Contribution of different aerosol species to the global aerosol extinction optical thickness: Estimates from model results. *Journal of Geophysical Research: Atmospheres*, 102(D20):23895–23915, October 1997.

[27] Bruce T. Draine and Piotr J. Flatau. Discrete-Dipole Approximation For Scattering Calculations. *Journal of the Optical Society of America A*, 11(4):1491, April 1994.

[28] Michael J. Iacono, Eli J. Mlawer, Shepard A. Clough, and Jean-Jacques Morcrette. Impact of an improved longwave radiation model, RRTM, on the energy budget and thermodynamic properties of the NCAR community climate model, CCM3.

Journal of Geophysical Research: Atmospheres, 105(D11):14873–14890, June 2000.